Journal of Fluids and Structures 28 (2012) 20–39

Contents lists available at SciVerse ScienceDirect

Journal of Fluids and Structures

journal homepage: www.elsevier.com/locate/jfs

Predictability of unsteady two-dimensional $k-\varepsilon$ model on the aerodynamic instabilities of some rectangular prisms

Kenji Shimada [a,*], Takeshi Ishihara [b]

[a] Institute of Technology, Shimizu Corporation, 3-4-17 Etchujima, Koto-ku, Tokyo 135-8530, Japan
[b] Department of Civil Engineering, School of Engineering, The University of Tokyo, 7-3-1, Hongou, Bunkyo-ku, Tokyo 113-8656, Japan

ARTICLE INFO

Article history:
Received 31 March 2010
Accepted 28 August 2011
Available online 26 October 2011

Keywords:
Computational fluid dynamics
$k-\varepsilon$ model
Vortex-induced-vibration
Torsional-flutter
Galloping
Aerodynamic instability

ABSTRACT

It is well known that a bluff body cross-section exhibits various kinds of aerodynamic instabilities such as vortex-induced vibration, galloping and torsional flutter. Since these cross-sections are used in long-span bridges and tall buildings, it is important to predict their occurrence in wind resistant structural design. In this paper, the authors make a series of comparisons of unsteady wind forces, unsteady pressure distributions and free vibration responses between previously conducted studies and an unsteady two-dimensional k–ε model for rectangular cross-sections with cross-sectional ratios of 2 and 4 in a smooth uniform flow in order to verify computational predictability of aerodynamic instabilities. As a result, the computation successfully predicted the onset velocities and responses of these aerodynamic instabilities for these cross-sectional ratios, which are common to tall buildings and long bridges.

1. Introduction

In cross-sections of structures such as bridges and buildings, which are bluff against wind flow, the shear layer separated from the leading edge and its interaction with their after-body play important roles in the occurrence of aerodynamic instabilities. Fig. 1 shows relationships between cross-sectional ratio B/D, where B is the along-wind length and D is the cross-section depth, and aerodynamic instabilities (Takeuchi and Matsumoto, 1992). Based on flow patterns formed around stationary cross-sections, instabilities are classified into three types: "separated", "periodically reattaching" and "permanently reattaching". From Fig. 1, it is recognized that Karman-vortex-type vortex-induced vibration is inherent to all ratios of cross-sections, galloping is related to separated-type cross-sections, motion-induced-vortex vibration and torsional flutter are related to periodically reattaching cross-sections, and coupled flutter is inherent to permanently reattaching cross-sections.

In separated-type cross-sections, shear layers that are alternately separated from both leading edges interact in the wake and form a Karman vortex, which is a source of two-shear-layer-type instabilities, i.e. Karman-vortex-type vortex-induced vibration and galloping.

In the periodically-reattaching-type cross-sections, the separated shear layer reattaches to the side surfaces of the cross-section. This enhances the formation of strong roll-up of a separated shear layer near the leading edges by impinging-shear-layer instability, which is a seed of one-shear-layer-type instability, i.e. motion-induced-vortex vibration.

* Corresponding author. Tel.: +81 3 3820 6897; fax: +81 3 3820 5955.
E-mail address: shimaken@shimz.co.jp (K. Shimada).

0889-9746/$ - see front matter © 2011 Elsevier Ltd. All rights reserved.
doi:10.1016/j.jfluidstructs.2011.08.013

Nomenclature

B	along-wind length of a body
C_{p_I}	out-of-phase component of unsteady wind pressure coefficient
C_{p_R}	in-phase component of unsteady wind pressure coefficient
C_{L_I}	out-of-phase component of unsteady lift coefficient
C_{L_R}	in-phase component of unsteady lift coefficient
C_{M_I}	out-of-phase component of unsteady pitching moment coefficient
C_{M_R}	in-phase component of unsteady pitching moment coefficient
D	cross-section depth
f_0	natural frequency
f_m	excitation frequency
h	damping decrement
$\eta(t)$	excitation amplitude
H	span length of a body
I	mass moment of inertia
m	mass
Sc	Scruton number or mass-damping ratio $=2m/(\rho BDH)2\pi h$ for transverse motion and $=2I/(\rho B^2D^2H)2\pi h$ for torsional motion
U_0	inflow velocity
U_r	reduced velocity $=U_0/(f_0B)$
W_r	normalized work
x	along-wind coordinate
y	transverse displacement
β	phase of unsteady force
β_p	phase of unsteady wind pressure
θ	torsional displacement
ρ	density of air

In stationary-reattachment-type cross-sections, the separated shear layer also reattaches to the side of the cross-section and forms a separated bubble. In the vibrating regime, the distance between the vibration center and the peak of the pressure fluctuation inside the separation bubble determines the difference in flutter derivatives [see, e.g., Matsumoto et al. (1997)].

Thus, the flow regimes around the stationary cross-section are closely related to the aerodynamic instabilities through the reattachment of the separated shear layer and the shear-layer instability.

Among these instabilities, for galloping and Karman-vortex-type transverse vortex-induced vibration, response can be predicted by means of a mathematical model such as quasi-steady theory (Parkinson and Wawzonek, 1981) and a nonlinear wake-oscillator model (Tamura and Shimada, 1987). With these models, once empirical parameters are identified from experiment, not only the onset velocity but also their response amplitudes can be predicted. For torsional motion, unlike transverse motion, although onset velocity can be predicted by Shiraishi and Matsumoto (1982) and Kubo et al. (1992), a mathematical model has not been developed yet [see, e.g., Païdoussis et al. (2011)]. On the other hand, computational fluid dynamics has recently been applied to the simulation of flow past a bluff body and aerodynamic force [see, e.g., Nomura (1994)]. However, so far there have been relatively few studies on application to the prediction of response [see, e.g., Kato (1997) and Tamura and Itoh (1998)] compared with those on unsteady wind forces [see, e.g., Kuroda (2000), Larsen and Walther (1998), Sarwar et al. (2008), and Shirai and Ueda (2003)].

In the evaluation of aeroelastic vibration it is necessary to conduct a calculation that consists of some hundred to a thousand of reduced time. Furthermore, since various reduced velocities should be examined with respect to changing mechanical properties such as mass-damping ratio, a parametric study by means of 3-D simulation requires enormous

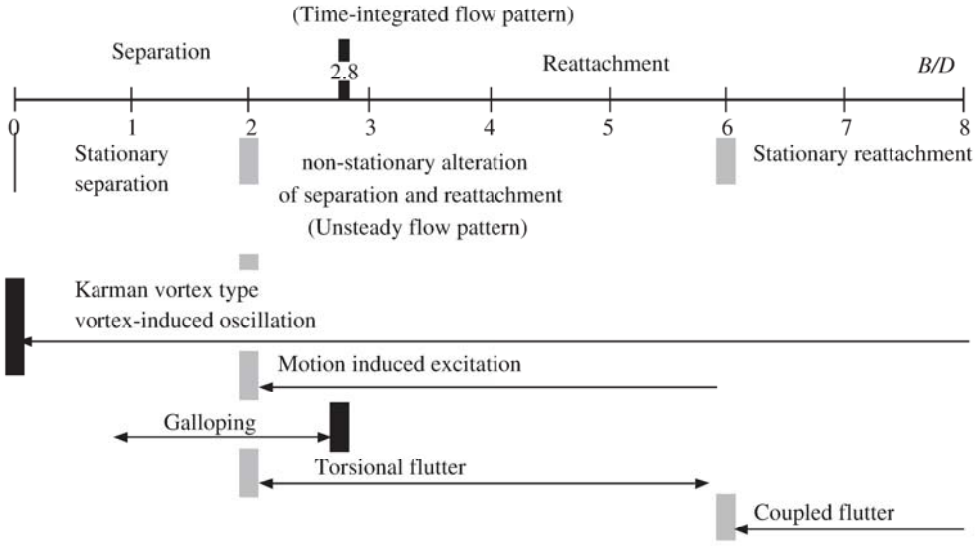

Fig. 1. Flow pattern of stationary cross-sections and aerodynamic instabilities (Takeuchi and Matsumoto, 1992).

computational time. However, by means of two-dimensional analysis, the authors have examined a k–ε model for prediction of aerodynamic characteristics of stationary rectangular cross-section (Shimada and Ishihara, 2001). In the high Reynolds number region, although three-dimensionality of the flow can not be neglected, the good performance of 2-D analysis is due to the turbulence viscosity produced by the implemented turbulence model or numerical dissipation, which act as a mimic spanwise momentum diffusion. This feature is extraordinarily advantageous for solving problems of aeroelastic vibration, which require a lot of computational time. However, two-dimensional analysis is essentially an approximation and thus it is necessary to examine the physical consistency of the obtained results. This paper examines the k–ε model for various types of aerodynamic instability by comparison with experiments. It then discusses the applicability of an unsteady two-dimensional k–ε model to the prediction of these instabilities based on the experimental results.

This paper consists of six sections. Section 2 describes the numerical methodology of fluid analysis incorporating aeroelastic motion and identification of unsteady wind forces. Section 3 explains in detail the experimental methodology of free vibration tests conducted to verify the numerical simulation. Section 4 compares analysis and experiments for transverse vibrations for $B/D=2$ and $B/D=4$ cross-sections, and discusses motion-induced-vortex vibration and transitional vibration to galloping. Section 5 compares torsional vibrations, and discusses motion-induced-vortex vibration in torsional mode and torsional flutter. Finally, Section 6 gives conclusions obtained from this study.

2. Numerical method

2.1. Fluid analysis

Numerical analysis is based on the two-dimensional unsteady k–ε model

$$\frac{DU_i}{Dt} = -\frac{\partial}{\partial x_i}\left(P+\frac{2}{3}k\right)+\frac{\partial}{\partial x_j}\left[(\nu+\nu_t)\left(\frac{\partial U_i}{\partial x_j}+\frac{\partial U_j}{\partial x_i}\right)\right]. \tag{1}$$

Here, subscripts on variables i and j (i, $j=1$, 2) follow Einstein's convention. In Eq. (1), the left hand side expresses a substantial derivative. If the body vibrates at a velocity $\dot{x}_j$, substantial derivative of quantity ϕ can be expressed as

$$\frac{D\phi}{Dt} = \frac{\partial\phi}{\partial t}+(U_j-\dot{x}_j)\frac{\partial\phi}{\partial x_j}, \tag{2}$$

ν_t is the eddy viscosity coefficient and is given as $\nu_t=C_\mu k/\varepsilon$. The turbulent kinetic energy k and its dissipation rate ε are obtained by the following their transport equations:

$$\frac{Dk}{Dt} = \frac{\partial}{\partial x_j}\left\{\left(\nu+\frac{\nu_t}{\sigma_k}\right)\frac{\partial k}{\partial x_j}\right\}+P_k-\varepsilon, \tag{3}$$

$$\frac{D\varepsilon}{Dt} = \frac{\partial}{\partial x_j}\left\{\left(\nu+\frac{\nu_t}{\sigma_\varepsilon}\right)\frac{\partial \varepsilon}{\partial x_j}\right\}+(C_{\varepsilon_1}P_k-C_{\varepsilon_2}\varepsilon)\frac{\varepsilon}{k}. \tag{4}$$

All of the empirical parameters in this equation, i.e. C_μ, C_{ε_1}, C_{ε_2}, σ_k and σ_ε are identical to those used in the conventional standard $k-\varepsilon$ model. P_k is the production of turbulent kinetic energy. In the present analysis a model proposed by Kato and Launder (1993), in which the production term is modified based on the assumption of flow irrotationality, is employed in order to prevent excessive production of turbulent kinetic energy near the leading edge:

$$P_k = C_\mu\frac{k^2}{\varepsilon}\sqrt{\frac{1}{2}\left(\frac{\partial U_i}{\partial x_j}+\frac{\partial U_j}{\partial x_i}\right)^2}\sqrt{\frac{1}{2}\left(\frac{\partial U_i}{\partial x_j}-\frac{\partial U_j}{\partial x_i}\right)^2}. \tag{5}$$

Since turbulence viscosity of flow in the vicinity of the wall boundary is smaller than in other areas, the above turbulence model is not applicable to this region. Therefore, there are alternatives such as imposition of a logarithmic law profile or a low Reynolds number model. The present method employs a two-layer model (Norris and Reynolds (1975) and Rodi (1991)) in the vicinity of the boundary:

$$\varepsilon = \frac{k^{3/2}}{l_\varepsilon}, \tag{6a}$$

$$\nu_t = C_\mu k^{3/2} l_\mu, \tag{6b}$$

here, length scales l_ε and l_μ are expressed as

$$l_\varepsilon = \frac{C_l y_w}{1+5.3/\mathrm{Re}_y}, \tag{7a}$$

$$l_\mu = C_l y_w\left\{1-\exp\left(-\frac{\mathrm{Re}_y}{A_\mu}\frac{25}{A^+}\right)\right\}, \tag{7b}$$

where constants in the above expressions, $C_l=0.41C_\mu^{-3/4}$, $A_\mu=50.5$ and $A^+=25$. y_w expresses the distance from the wall. In the two-layer model, since l_ε and l_μ are the functions of turbulent Reynolds number $\mathrm{Re}_y(=k^{1/2}y_w/\nu)$, Reynolds number

effect of the flow can be taken into account. Although this methodology requires more grid points near the wall than the logarithmic law, it can resolve the flow well when the flow reattaches to the wall. Furthermore, since ε is imposed algebraically by Eq. (6a) near the wall boundary, complicated treatment near the wall such as a low Reynolds number model can be avoided. In the present calculation, the two-layer model is applied only to the region within three meshes from the solid boundary.

The pressure $P=p/\rho$ is obtained by solving the Poisson equation, given as

$$\nabla^2 P = -\frac{\partial}{\partial x_i}\left\{(U_j-\dot{x}_j)\frac{\partial U_i}{\partial x_j}\right\}+\frac{\partial}{\partial x_i}\left[\frac{\partial}{\partial x_j}\left\{\nu_t\left(\frac{\partial U_i}{\partial x_j}+\frac{\partial U_j}{\partial x_i}\right)\right\}\right]+\frac{\nabla_i U_i}{\Delta t}. \tag{8}$$

In order to simulate the flow fields around a bluff body, the separated shear layer should be resolved accurately. For this purpose, a body-fitted coordinate system is employed to concentrate grids near the bluff body (Fig. 2). The above set of equations is transformed into analytical space from physical space by using a generalized coordinate system. A set of transformed equations are discretized by the finite difference method. The Marker and Cell Method by Harlow and Welch (1965) is employed for the time marching with a modification of the arrangement of variables. In the present analysis, a regular grid is used, that is, all dependent variables are located on the same grid points. The convective terms in the momentum transport equation are approximated by the third-order upwind difference scheme by Kawamura and Kuwahara (1984), and the convective terms in the k and ε transport equations are discretized by the first-order upwind difference scheme to stabilize the numerical instability at high Reynolds number arising from the nonlinear effect of the convective term. Numerical grids are generated by an O-type grid system and the number of grid points is $320\times 200=64\,000$. In order to simulate the structure's motion, the analytical domain is divided into an inner region and a perimeter region (Fig. 3). The latter is fixed and the former moves with the structure. A buffer region is made between them, where the grids of the inner and perimeter zones are connected. The Reynolds number is chosen to be $\mathrm{Re}=U_0D/\nu=22\,000$, where U_0 is the inflow velocity and ν is the kinematic viscosity, so as to be consistent with the order of the Reynolds number in the experiments. Reduced wind speed $U_r=U_0/(fB)$ is adjusted by sweeping the frequency.

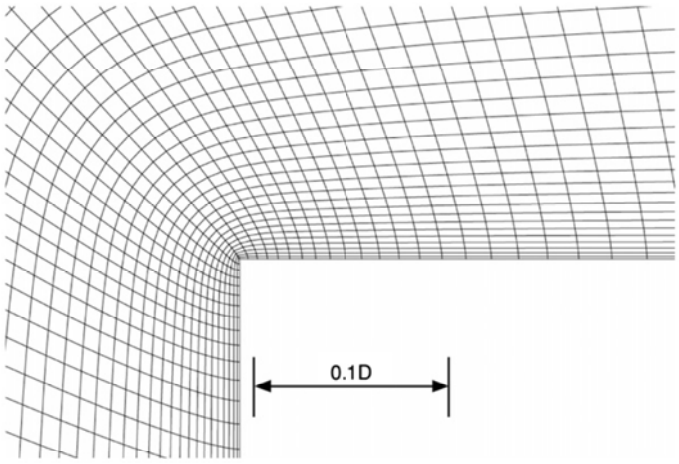

Fig. 2. Grid in the vicinity of a cross-section.

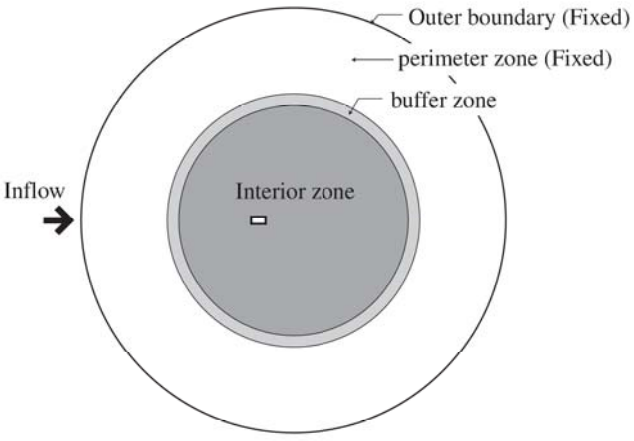

Fig. 3. Schematic of analytical domain.

2.2. Forced vibration

2.2.1. Unsteady wind force

In this section, numerical calculation of forced vibration for one-degree-of-freedom transverse and torsional motion is explained. At first, the displacement motion of the forced vibration is assumed to be expressed as

$$\eta(t) = \eta_0 \sin \omega_m t, \tag{9}$$

where $\eta(t)$ expresses forced motion, which is transverse motion in Section 4 and rotational angle in Section 5. Dominant components of unsteady wind force are a vortex-shedding component and a forced frequency component. The latter has a delay from forced motion and is expressed as

$$F_m(t) = F_0 \sin(\omega_m t + \beta), \tag{10}$$

where F_m expresses unsteady wind force, which is unsteady lift in Section 4 and unsteady pitching moment in Section 5. ω_m is circular frequency ($=2\pi f_m$) and F_0 is the amplitude of unsteady wind force. F_0 and β are expressed by Fourier decomposition of the aerodynamic forces obtained by fluid analysis as

$$F_0 = \sqrt{F_{m_l}^2 + F_{m_R}^2}, \quad \beta = \tan^{-1} F_{m_l}/F_{m_R}, \tag{11a}$$

$$\{F_{m_l}, F_{m_R}\} = \frac{2}{T}\int_{-T}^{T} F_m(t)[\cos \omega_m t, \sin \omega_m t]\,dt, \tag{11b}$$

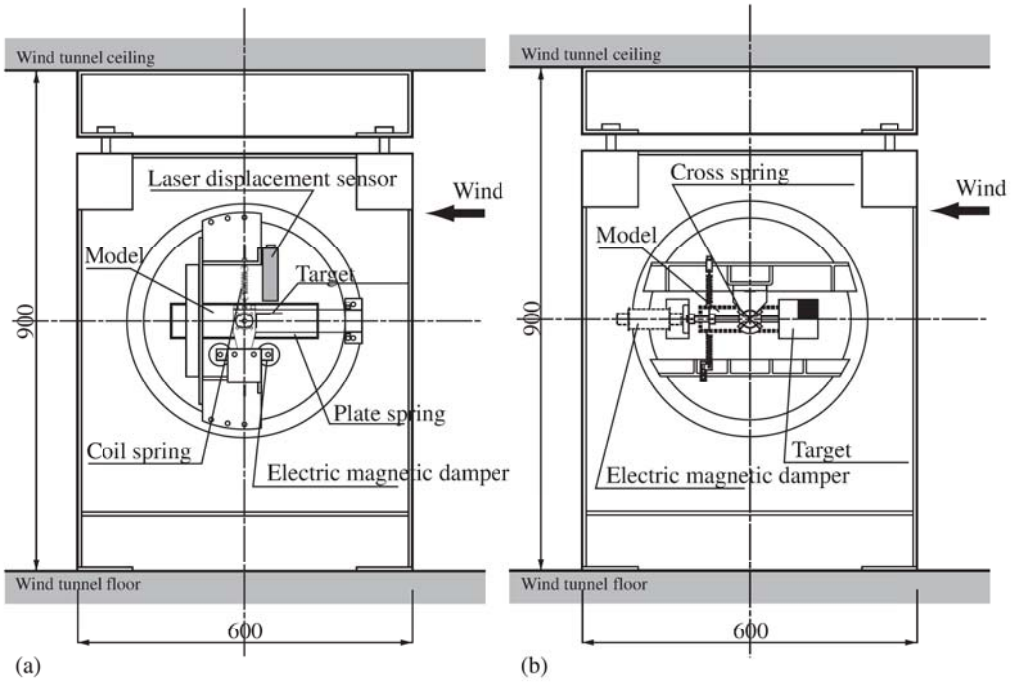

Fig. 4. Experimental apparatus for free vibration test: (a) transverse mode and (b) torsional mode.

Table 1
Mechanical properties of experimental model in transverse mode.

Case	B/D	$B \times D \times H$ (mm)	f_0 (Hz)	m (kg)	h (%)	Sc
1	4	$120 \times 30 \times 300$	10.3	0.256	0.13	3.2

Table 2
Mechanical properties of experimental model in torsional mode.

Case	B/D	$B \times D \times H$ (mm)	f_0 (Hz)	m (kg)	h (%)	Sc
2	2	$80 \times 40 \times 300$	21.5	5.09×10^{-4}	0.29–0.44	4.9–7.5
3	2	$80 \times 40 \times 300$	9.175	3.12×10^{-3}	0.44–0.52	45.8–54.1
4	4	$120 \times 30 \times 300$	19.15	6.91×10^{-4}	0.24–0.63	4.4–11.5

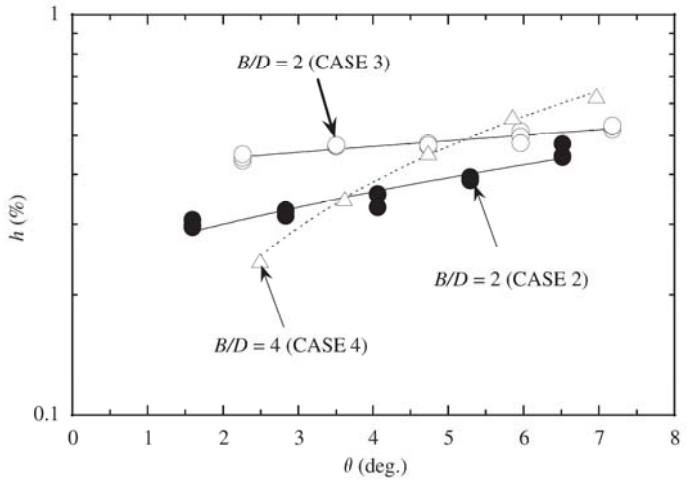

Fig. 5. Dependence of damping decrement on amplitude in torsional mode.

Table 3
Mechanical properties of a $B/D=2$ cross-section in transverse mode.

DATA	Sc	Mass ratio $2m/(\rho BDH)$	Logarithmic damping
Miyazaki (1982)	3.0	750	0.0040
Takeda and Kato (1992)	1.6	302	0.0053
$k-\varepsilon$ model	2.0	500	0.0040

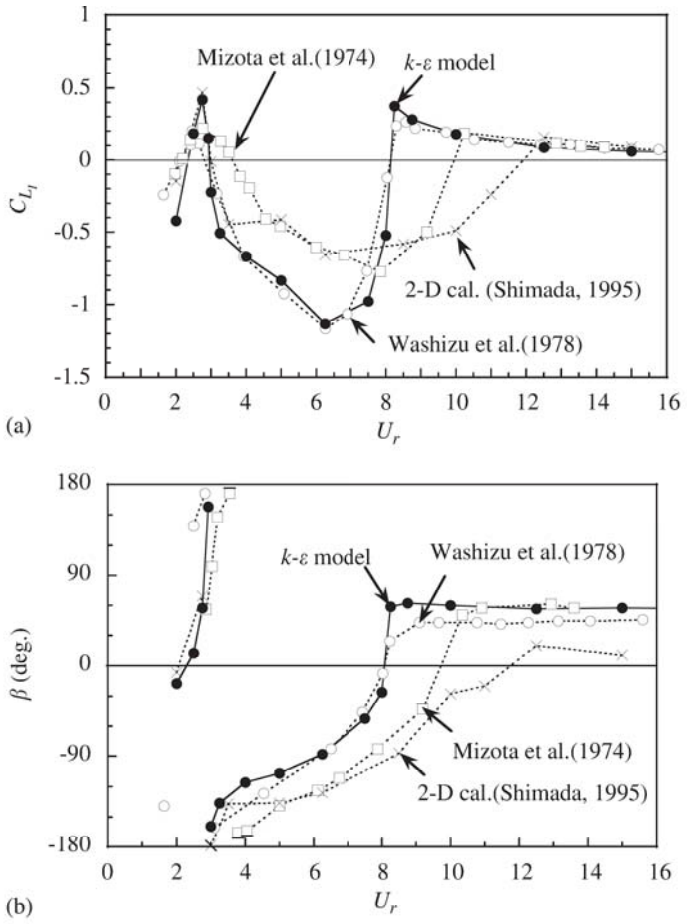

Fig. 6. Unsteady lift coefficient of a $B/D=2$ cross-section in transverse mode with $y_0/D=0.1$: (a) out-of-phase component and (b) phase.

where $T=N/f_m(N\geq 1)$. Therefore, the unsteady forces can be decomposed as

$$F_m(t)=F_{m_R}\sin\omega_m t+F_{m_I}\cos\omega_m t, \tag{12a}$$

$$F_{m_R}=F_0\cos\beta,\quad F_{m_I}=F_0\sin\beta, \tag{12b}$$

where the first term on the right hand side of Eq. (12a) F_{m_R} is called the in-phase component and the second term F_{m_I} is called the out-of-phase component. F_{m_I} plays an important role on the stability of the vibration. When the above aerodynamic forces are applied to a body of a structure, the equation of motion becomes

$$m\ddot{\eta}+c\dot{\eta}+k\eta=F_m(t)=F_{m_R}\frac{\eta}{\eta_0}+F_{m_I}\frac{\dot{\eta}}{\omega_m\eta_0}. \tag{13}$$

Since the second term on the right hand side is in phase with damping force, it is called aerodynamic damping. When $F_{m_I}>0$, i.e. $F_0>0$ and $\beta=90^\circ$, it acts to decrease the structural damping force, and is called aerodynamic negative damping. Since the in-phase component is the same phase as the restoring force, it is called aerodynamic stiffness. These forces are expressed as coefficients as

$$C_{L_R}-\frac{L_{m_R}}{(1/2)\rho U^2 B},\quad C_{L_I}-\frac{L_{m_I}}{(1/2)\rho U^2 B}, \tag{14a}$$

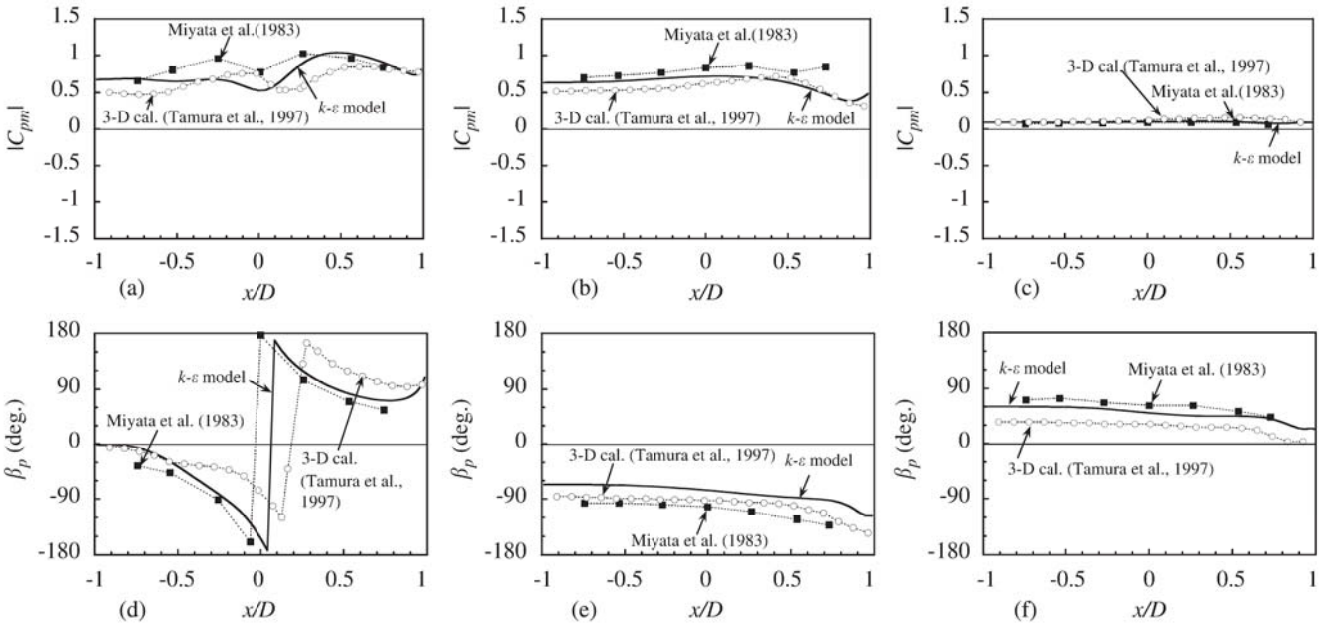

Fig. 7. Unsteady pressure distribution of a $B/D=2$ cross-section in forced transverse vibration mode with $y_0/D=0.1$: (a) $|C_{p_m}|$ ($U_r=2.75$), (b) $|C_{p_m}|$ ($U_r=6.75$), (c) $|C_{p_m}|$ ($U_r=12.0$), (d) phase ($U_r=2.75$), (e) phase ($U_r=6.75$), and (f) phase ($U_r=12.0$).

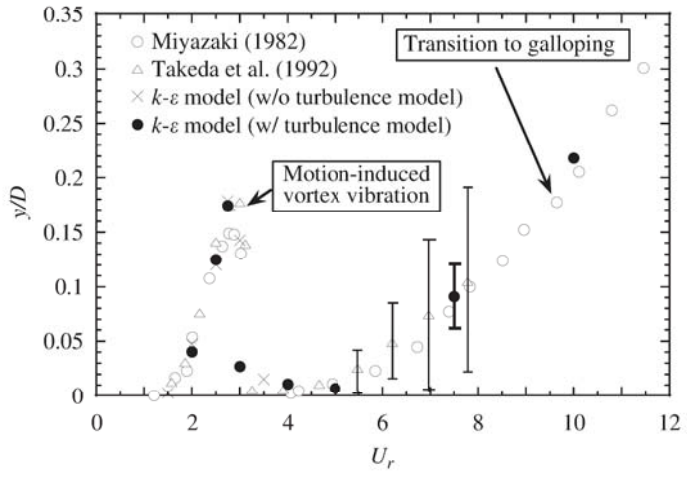

Fig. 8. Normalized response of a $B/D=2$ cross-section in free transverse vibration mode.

$$C_{M_R} = \frac{M_{m_R}}{(1/2)\rho U^2 B^2}, \quad C_{M_I} = \frac{M_{m_I}}{(1/2)\rho U^2 B^2}, \tag{14b}$$

where L_{m_R}, L_{m_I} and M_{m_R}, M_{m_I} are in-phase and out-of-phase components of unsteady lift and pitching moment of unit span length. The unsteady wind forces are functions of frequency and amplitude of motion.

2.2.2. Unsteady pressure

The same definition can be established for the fluctuating pressure. The unsteady pressure coefficients can be defined as

$$C_{p_R} = \frac{p_{m_R}}{(1/2)\rho U^2}, \quad C_{p_I} = \frac{p_{m_I}}{(1/2)\rho U^2} \tag{15a}$$

$$|C_{p_m}| = \sqrt{C_{p_R}^2 + C_{p_I}^2}, \quad \beta_p = \tan^{-1} C_{p_I}/C_{p_R} \tag{15b}$$

$$p_{m_R} = p_0 \cos\beta_p, \quad p_{m_I} = p_0 \sin\beta_p, \tag{15c}$$

where C_{p_R} and C_{p_I} are the in-phase and out-of-phase components of the fluctuating pressure coefficients. They give spatial information of excitation source. When a portion on the surface of a structure is $C_{p_I} > 0$, i.e. $|C_{p_m}| > 0$ and $\beta_p = 90°$, it means that the fluctuating pressure at the portion is an exciting source.

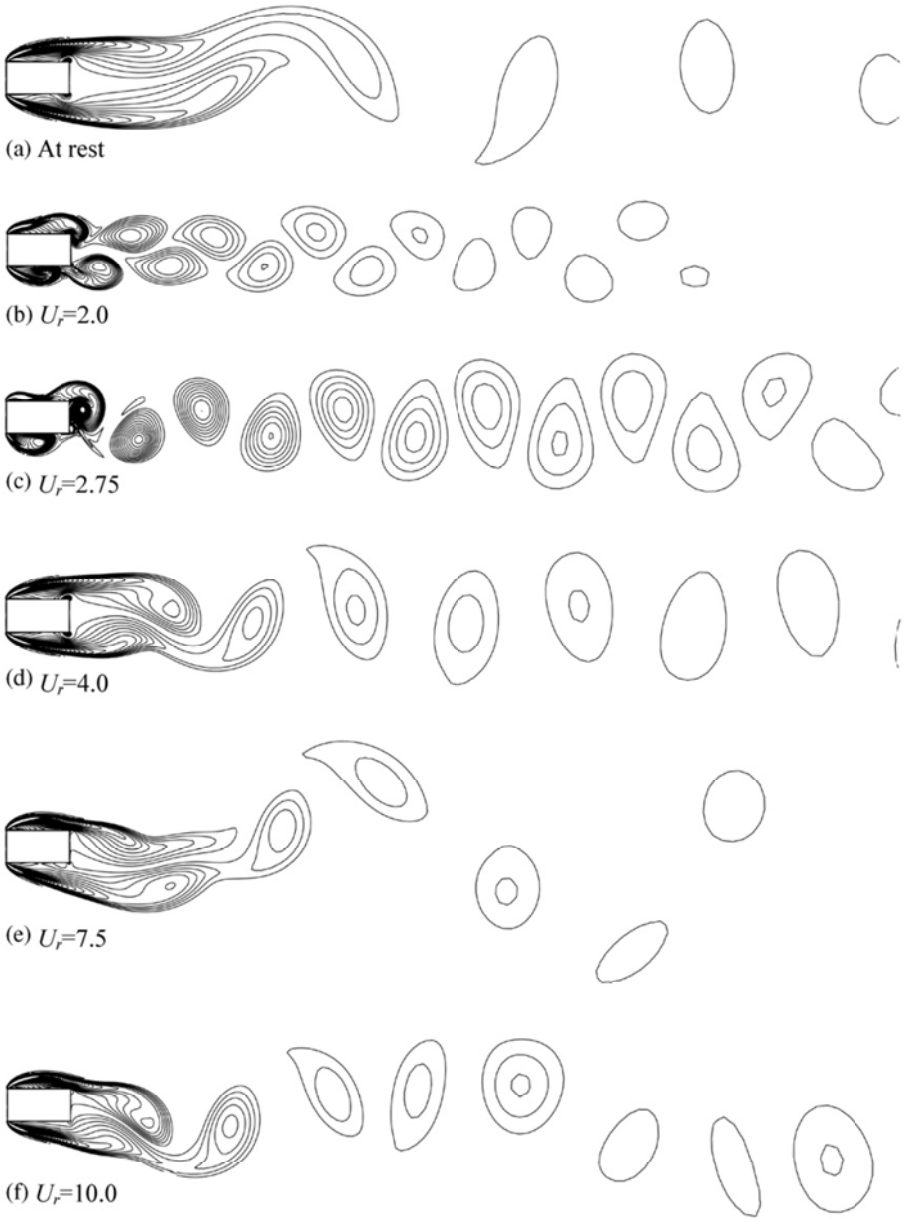

Fig. 9. Instantaneous vorticity field of a $B/D=2$ cross-section in transverse free vibration at its maximum amplitude except for (a): (a) at rest, (b) $U_r=2.0$, (c) $U_r=2.75$, (d) $U_r=4.0$, (e) $U_r=7.5$, and (f) $U_r=10.0$.

2.3. Free vibration

For free vibration, instead of assigning a motion of a body by Eq. (9) a priori, motion of a body is obtained by solving the equation of motion. In both cases, the incidental velocity vector relative to a body is detected locally from free stream flow velocities and motion velocities automatically.

3. Free vibration test methodology

One-degree-of-freedom transverse and torsional free vibration tests were conducted to verify the numerical results. Fig. 4 shows the experimental apparatus. These motions were realized by a pair of springs comprising a plate spring for transverse motion and a cross-spring for torsional motion. Damping was added by an electronic magnetic damper. Transverse displacement was measured by an optical displacement sensor. Torsional displacement was obtained by dividing the target displacement by the length between the target and the center of rotation. The experimental results showed sinusoidal motion, but in this paper results are shown as their standard deviation multiplied by $\sqrt{2}$. Experiments were conducted using models made as light as possible. The experimental model was made of balsa. At both sides of the model tips, end plates made of aluminum were attached. Tables 1 and 2 list the parameters of the experimental model. Fig. 5 shows the variation of damping coefficient. A slight dependence on the amplitude of motion is observed (Table 3).

4. One-degree-of-freedom transverse motion

4.1. Unsteady lift of $B/D=2$ cross-section

The $B/D=2$ cross-section is attractive from the engineering as well as from the numerical analysis point of view since it exhibits both galloping and motion-induced-vortex vibration, which are typical of separated- and reattaching-type cross-sections. Fig. 6 shows numerical results of unsteady lift force coefficient C_{L_l} obtained as a result of forced vibration in the transverse mode with an amplitude of $y_0/D=0.1$. C_{L_l} becomes positive in the region near $U_r=2.5$ and $U_r>7.5$, where motion-induced-vortex vibration and galloping occur, respectively. Computational results also corresponded with the experimental results by Washizu et al. (1978).

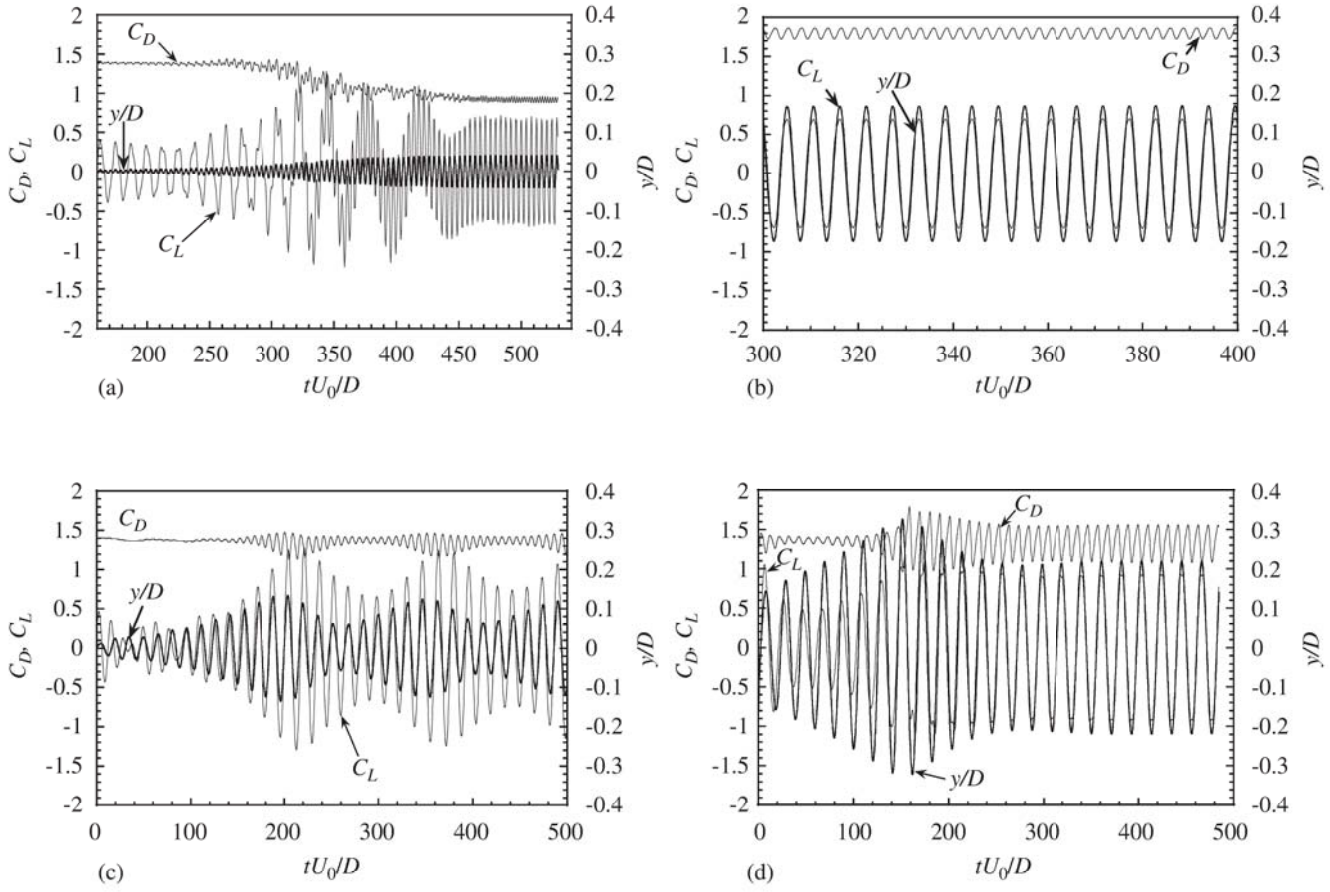

Fig. 10. Time histories of a $B/D=2$ cross-section in transverse free vibration: (a) $U_r=2.0$, (b) $U_r=2.75$, (c) $U_r=7.5$, and (d) $U_r=10.0$.

It is worth mentioning that when we use an ordinary 2-D analysis that simply neglects the spanwise velocity component without incorporating a turbulence model, the lower range of reduced velocity is well reproduced but the higher region can not be simulated (Shimada, 1995).

Fig. 7 shows unsteady pressure distributions on the surface of the cross-section for U_r=2.75, 6.75 and 12.0. At U_r=2.75, β_p is out of phase on the leeward side ($x/D>0$), which means that C_{p_l} is positive, so an exciting force acts on the leeward side. At U_r=6.75, where $|C_{p_m}|>0$ and $\beta_p<0$, i.e. $C_{p_l}<0$ on the whole region of the surface, the damping force acts on the cross-section when y_0/D=0.1. At U_r=12, where $|C_{p_m}|\cong 0|$ and $\beta_p>0$, C_{p_l} recovers slightly from U_r=6.75 and transition to galloping begins appearing. The figure also shows experimental results by Miyata et al. (1983) and three-dimensional numerical analysis by Tamura and Itoh (1997), and the present results agree well with those results.

4.2. Simulation of transversely elastically supported B/D=2 cross-section

Scruton number (Sc=$2m/(\rho BDH)2\pi h$, where H: spanwise length, m: mass, h: damping ratio, ρ: air density) is a dominant parameter in vortex-induced vibration. According to the quasi-steady theory by Parkinson and Wawzonek (1981), galloping depends on the mass ratio and damping decrement independently. Therefore, in order to perform an analysis in a reduced velocity range from vortex-induced vibration to galloping transition, information is required on both mass and damping.

Fig. 8 shows transverse elastically supported response. Fig. 9 shows the instantaneous vorticity field at the instant of maximum amplitude for some typical reduced velocities. Also, Fig. 10 shows drag, lift and displacement time series during the motion.

Fig. 10(a) shows drag, lift and response for U_r=2 where the cross-section is first at rest. At first, lift fluctuates with Strouhal number frequency. However, at tU_0/D=275, a forced vibration frequency component appears. At tU_0/D=450, the former component is replaced by the latter component. Vortex shedding is synchronized with the motion, and the flow pattern shown in Fig. 9(b) is completely different from the flow at rest in Fig. 9(a).

At U_r=2.75, motion-induced-vortex vibration is at its maximum amplitude. Mean drag and base pressure are larger than those for a stationary cylinder. This is because a strong secondary vortex is formed at the trailing edges of the cross-section.

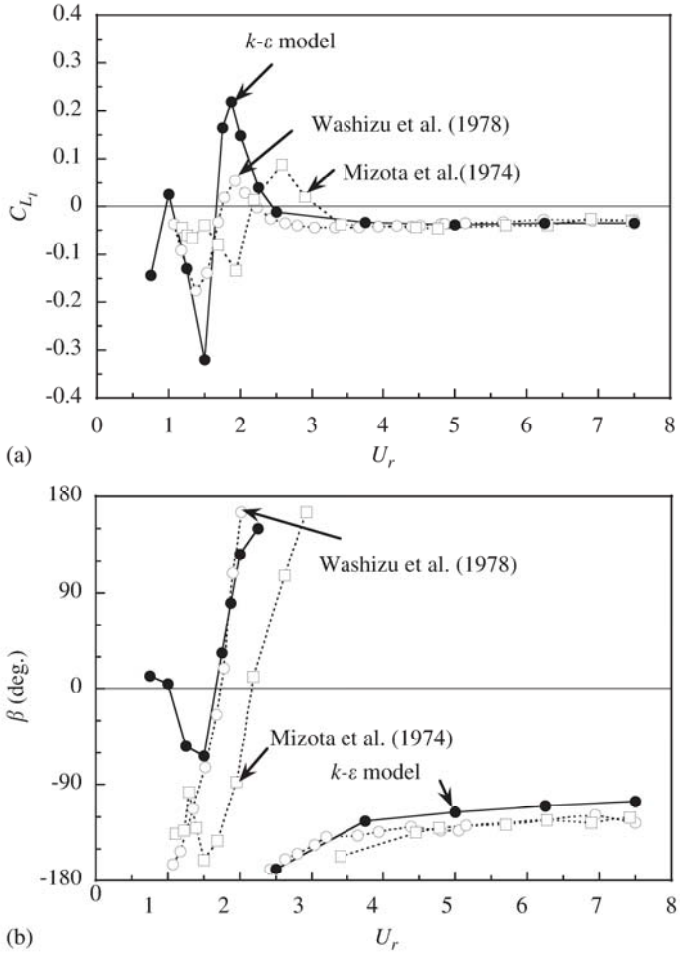

Fig. 11. Unsteady lift coefficient of a B/D=4 cross-section in transverse mode with y_0/D=0.02: (a) out-of-phase component and (b) phase.

This vortex is merged with the rolled up vortex traveling downstream along the side surfaces from the leading edge, and is shed into the wake. This flow pattern corresponds closely with that reported by Shiraishi and Matsumoto (1982).

At U_r=4.0, vortex shedding is out of synchronization, so the amplitude is abruptly reduced. From near U_r=5.0 the response resumes increasing. Since this reduced velocity almost coincides with the resonant velocity, which is defined as the reciprocal of the Strouhal number St=0.085, Karman-vortex-type vortex-induced vibration seems to be latently involved with it.

At U_r=7.5, the oscillation is found to be modulated as shown in Fig. 10(c). This modulation is also observed in the experiments by Takeda and Kato (1992) in Fig. 8, as indicated by the error bar. In this range of reduced velocities, since vortex shedding is involved, the phenomenon is complicated [see, e.g., Itoh and Tamura (2002)]. However, if the mass ratio and damping decrement are relatively small, the response transits to galloping. At U_r=10.0, as can be found in Fig. 9(f), it can be recognized that flapping of the separated shear layer plays an important role in the formation of aerodynamic force.

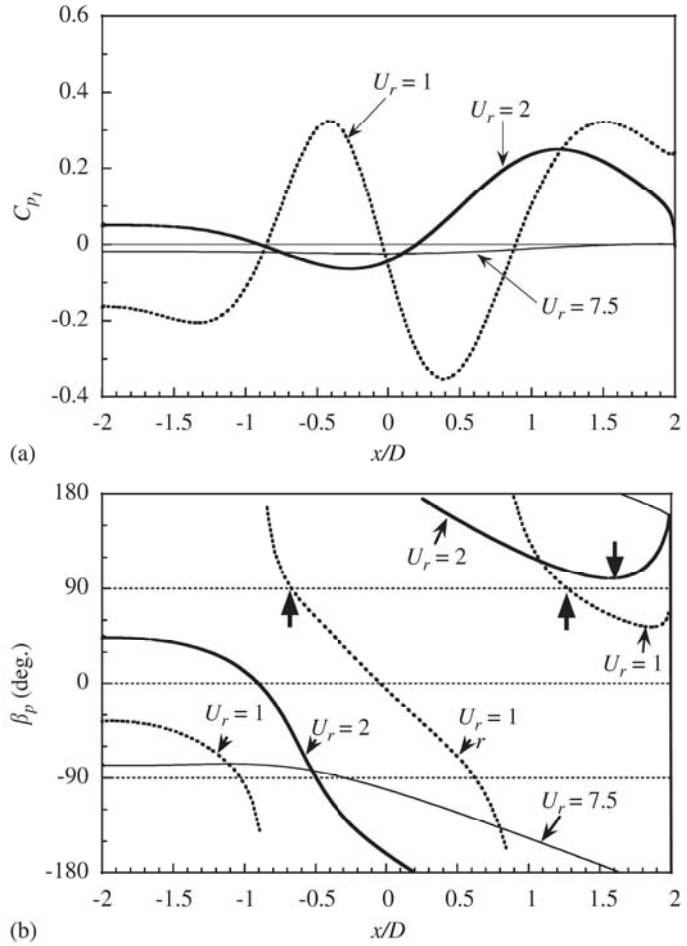

Fig. 12. Unsteady pressure distribution of a B/D=4 cross-section in forced transverse vibration mode with y_0/D=0.02: (a) out-of-phase component and (b) phase.

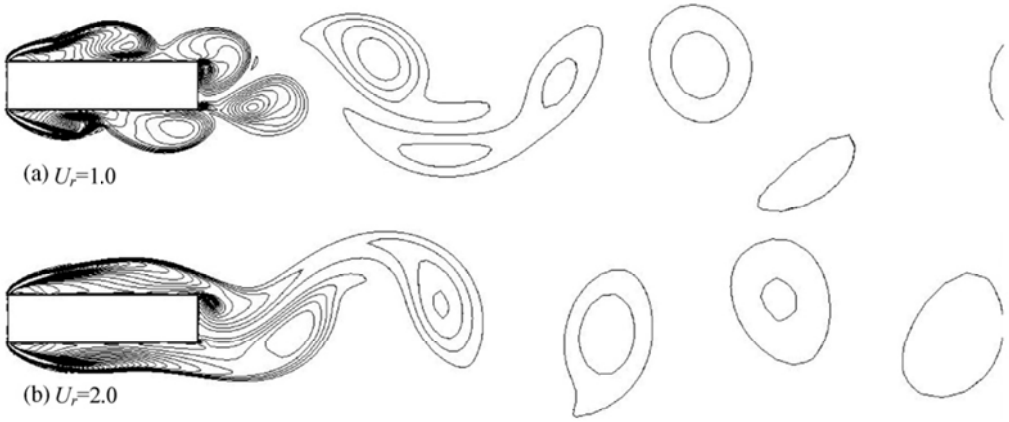

Fig. 13. Instantaneous vorticity field of a B/D=4 cross-section in transverse forced vibration with y_0/D=0.02 at its maximum lift.

4.3. Unsteady wind forces of $B/D=4$ cross-section

Cross-sections within the range of $B/D=3$–6 are classified into periodically reattaching-type cross-sections. These types of cross-sections exhibit multiple excitation peaks. In this section, numerical simulation is applied to this cross-section and its applicability is verified.

Fig. 11 compares unsteady wind force with the experimental results by Mizota and Nakamura (1974) and Washizu et al. (1978). In Fig. 11(a), C_{L_l} becomes positive near $U_r=1$ and $U_r=1.75$. Although the magnitude of the peak calculated by the simulation is slightly larger than the experimental value, including phase difference, the global characteristics are found to be in good agreement.

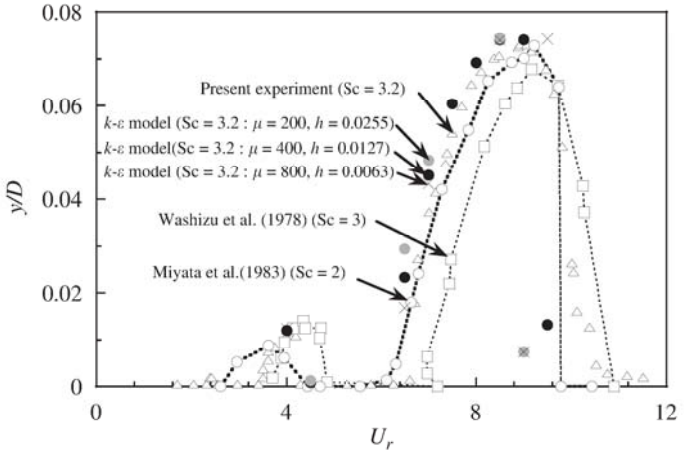

Fig. 14. Normalized response of a $B/D=4$ cross-section in free transverse vibration mode.

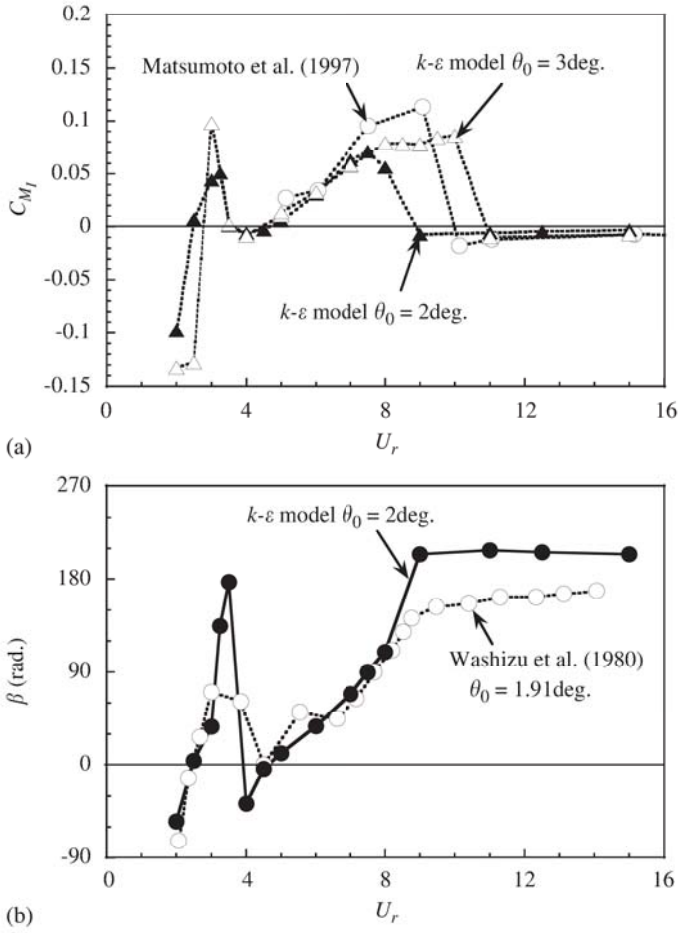

Fig. 15. Unsteady pitching-moment coefficients of a $B/D=2$ cross-section in torsional mode: (a) out-of-phase component and (b) phase.

Fig. 12 shows unsteady pressure distributions. At $U_r=1$ and $U_r=2$, C_{p_l} becomes positive on a couple of regions on the surface. However, since they are canceled by the negative portions, the total excitation force is smaller than for $U_r=2$. For $U_r=7.5$, C_{p_l} is negative over the whole of the surface. At $U_r=1$, the vorticity contour in Fig. 13 shows that there are always two apparent vortices on either side of the surface. For $U_r=2$, there is only one portion where C_{p_l} becomes positive and primal excitation force is generated there. In this case, Fig. 13 shows one large vortex on the surface.

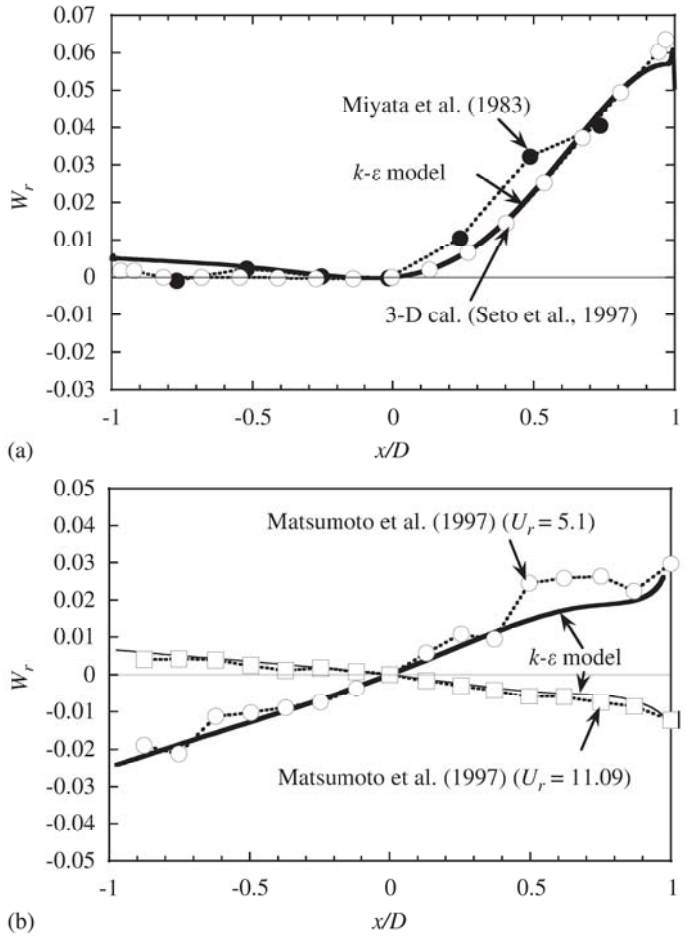

Fig. 16. Normalized work done by pressure of a $B/D=2$ cross-section in torsional forced vibration mode: (a) $U_r=3.0$ ($\theta_0=2^\circ$) and (b) $5.0<U_r<12.0$ ($\theta_0=3^\circ$).

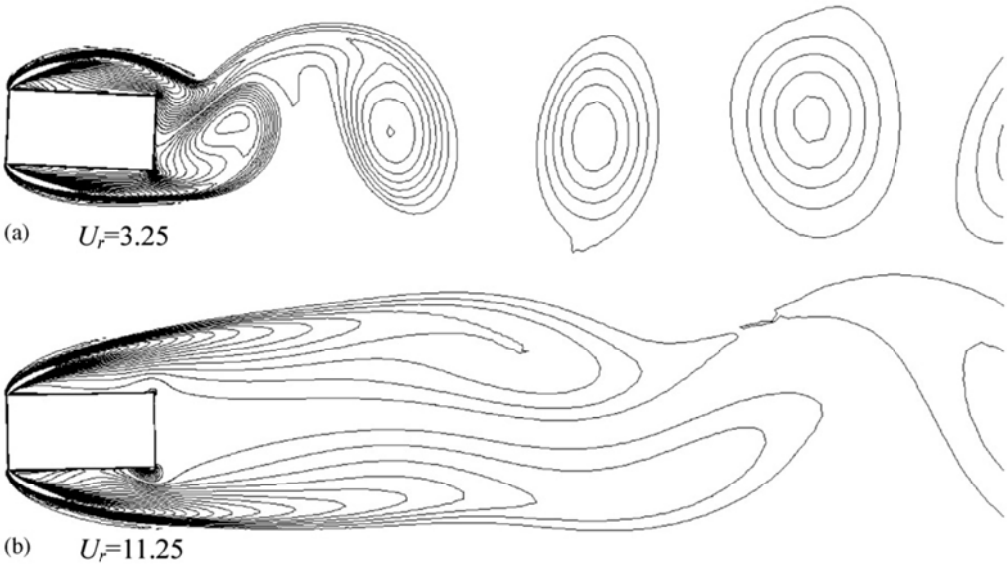

Fig. 17. Instantaneous vorticity field of a $B/D=2$ cross-section in torsional forced vibration with $\theta_0=3.82^\circ$.

4.4. Simulation of transversely elastically supported B/D=4 cross-section

Fig. 14 compares the numerical and experimental results of transverse free vibration of a $B/D=4$ cross-section by Washizu et al. (1978) and Miyata et al. (1983). In the V-A diagram, excitations are recognized at $U_r=1$ and $U_r=1.75$. Since these onset velocities can be predicted by the formula by Shiraishi and Matsumoto (1982) as $U_r=0.83$ and $U_r=1.67$, these excitations can be regarded as motion-induced-vortex vibration. Excitations are recognized within regions where C_{L_l} shows positive values in Fig. 11(a). For $U_r>2.75$, since C_{L_l} shows negative values, no excitations are recognized.

Scruton number (Sc) consists of the mass ratio $\mu=2m/(\rho BDH)$ and the damping decrement h. In order to see the effect of these parameters, in Fig. 14 the values are varied as the products are equal to Sc=3.2. Regardless of the value of the mass ratio and the damping decrement, the peak responses are almost the same. This result agrees with the findings by Tamura and Matsui (1979) where this is analytically shown by means of the wake-oscillator model in which the Karman-vortex-type vortex-induced vibration gives the same peak response if the Scruton number is the same.

5. One-degree-of-freedom torsional motion

5.1. Unsteady pitching moment of B/D=2 cross-section

In the unsteady pitching moment in Fig. 15, positive C_{M_l} is recognized in two regions, i.e. $U_r=3$ and $7.5<U_r<9$. Although in the experiment by Matsumoto et al. (1997) the amplitude is 2°, the numerical result is found to give better agreement when the amplitude is set to 3°.

Fig. 16 shows distributions of normalized work per unit area W_r on a surface.

$$W_r=-\frac{\pi x}{D}\sin\theta_0|C_{p_m}|\sin\beta_p. \tag{16}$$

In Fig. 16(a) at $U_r=3$, W_r is positive, and is especially large when $x/D>0$, which is the excitation source. The numerical results agree well with both the wind tunnel experiment by Miyata et al. (1983) and the three-dimensional numerical simulation by Seto et al. (1997).

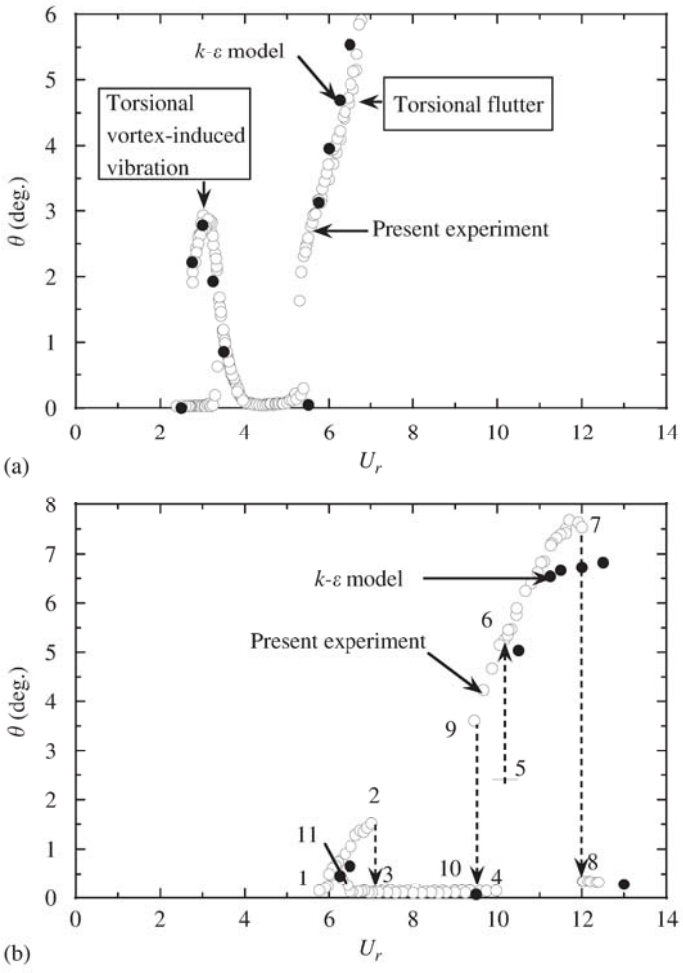

Fig. 18. Normalized response of a $B/D=2$ cross-section in torsional free vibration: (a) $4.9<Sc<7.5$ and (b) $46<Sc<54$.

Fig. 16(b) exhibits W_r for $U_r=5$ and 11. From Fig. 15(a), at each U_r, pitching excitation is almost zero. From W_r at $U_r=5$, the windward portion on the side surface becomes damping force and the leeward portion contributes as an excitation force, but, at $U_r=11$ the opposite applies. Since the sums of the integrated amounts on each side are almost the same, they cancel each other out, so the total excitation moments are small. The numerical results simulated these changes well with respect to the reduced windspeed.

Fig. 17 shows instantaneous vorticity fields for $U_r=3.25$ and $U_r=11.25$. At $U_r=3.25$, where excitation moment is arising, a vortex is formed behind the cross-section. At $U_r=11.25$, where excitation moment is small, the vortex formation is weak and is apart from the cross-section.

5.2. Simulation of rotationally elastically supported B/D=2 cross-section

Fig. 18 compares the free vibrations of the author's experiment with the numerical results. Both the relatively small Scruton number case and the large case are illustrated in Fig. 18(a) and (b), respectively, where Scruton number is defined as $Sc=2I/(\rho B^2D^2H)2\pi h$, where H: spanwise length, I: mass moment of inertia, h: damping decrement and ρ: air density. Although, as can be seen in Fig. 5, damping decrement has amplitude dependency, in the analysis, Scruton number is set to $Sc=5.5$ ($h=0.325\%$) and $Sc=50$ ($h=0.44\%$). The experiment shows the onset velocity of vortex-induced vibration at $U_r=2.75$ and torsional-flutter at $U_r=5.25$. The numerical results successfully simulated both the onset velocities and the peak amplitudes of these excitations.

Scruton number in Fig. 18(b) is larger where $Sc=50$ and $h=0.44\%$. From the experiment, two peaks are recognized in response, whose onset velocities are $U_r=6$ and 9.5. In the figure, response tracks are indicated by digit ordering. Response amplitude increases with U_r from point 1 to point 4. However, after point 4, there is no increase in amplitude in spite of increasing U_r. Tracks from point 6 to point 7 are obtained by initially imposing a certain amplitude 5. In the analysis, the response amplitude at this point was obtained in the same manner by assigning an initial amplitude of $\theta_0=3.82^\circ$. After this point, the response increases up to point 7 and then suddenly drops.

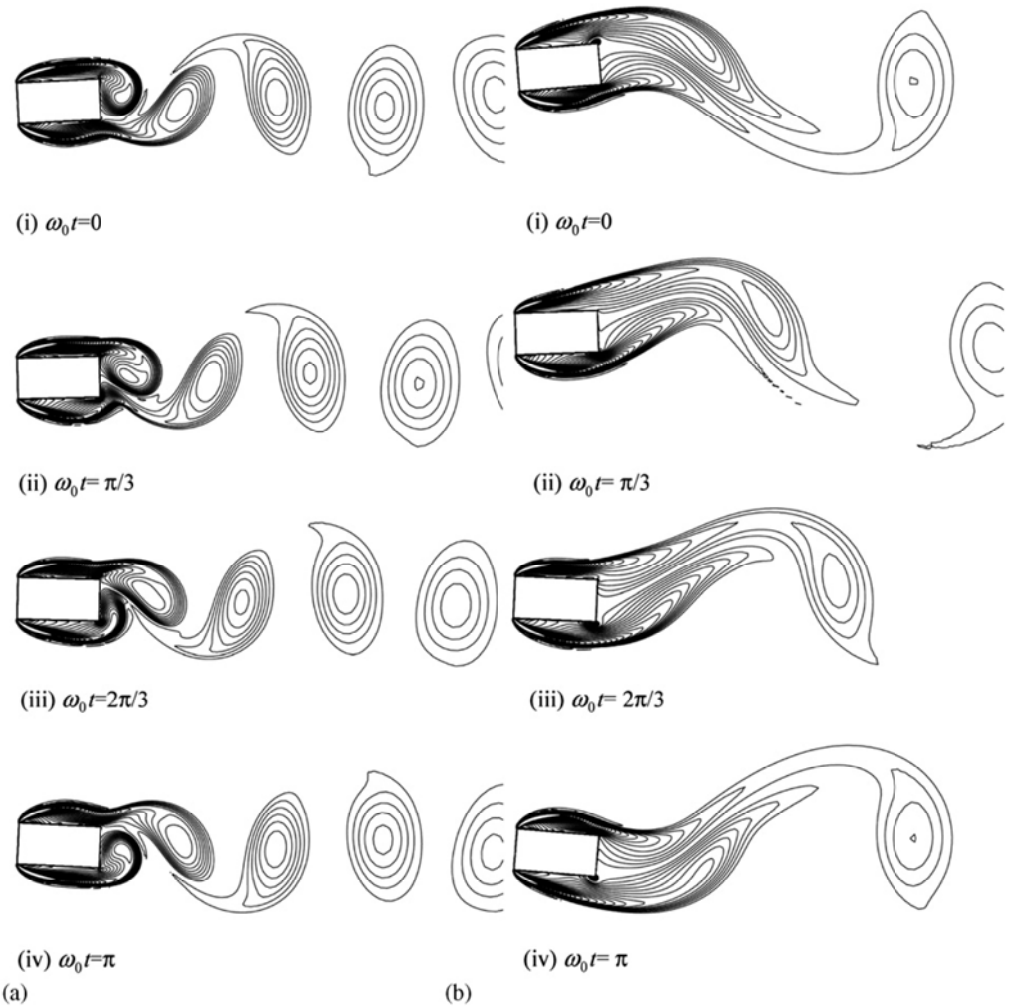

Fig. 19. Instantaneous vorticity field of a $B/D=2$ cross-section in torsional free vibration: (a) torsional vortex-induced-vibration ($U_r=3$) and (b) torsional flutter ($U_r=6.25$).

It is also suggested by Nakamura and Mizota (1975) and Washizu et al. (1980) that in the high reduced velocity region $U_r > 7$ there is a region where excitation moment is small if the amplitude is small. Thus, the response does not develop by itself unless a certain amount of initial amplitude is imposed. The response looks like a velocity-restricted-type vibration such as vortex-induced vibration, but its mechanism is not the same.

Fig. 19 shows instantaneous vorticity contours of half cycle at $U_r=3$ and 6.25 where vortex-induced vibration and torsional flutter occur. At the vortex-induced vibration, a separated shear layer rolls up into a vortex downstream of the cross-section and is shed into the wake. However, at the torsional flutter, no apparent rollup of the shear layer is observed near the cross-section. Instead, the vortex is shed into the wake away from the cross-section.

5.3. Unsteady pitching moment of $B/D=4$ cross-section

This section presents torsional vibration of a $B/D=4$ cross-section as a representative of a separated shear-flow-reattaching-type cross-section. Fig. 20 shows unsteady pitching moment coefficients. The amplitude of the numerical simulation is $\theta_0=3.82^\circ$ which is the same as in the experiment by Washizu et al. (1980). In the region $U_r > 5$, C_{M_I} is positive, which indicates that torsional flutter will occur. For C_{M_I}, the numerical simulation agrees well with the experiment over the whole reduced velocity region. However, for $U_r < 3$, C_{M_R} does not agree with the experiment. Since the period of the motion becomes short for lower U_r, the result of a fine time increment $\Delta t=1/2000$, which is 1/5 that of the usual cases, is also indicated for $U_r=1$ in the figure. However C_{M_R} is almost the same as that for usual Δt. Therefore, no difference is found due to the time increment. Although no figure is shown, the same characteristic is found for $B/D=2$ of the present simulation and a two-dimensional simulation of a $B/D=5$ cross-section by the third-order upwind difference by Tamura and Kuwahara (1992). In the present simulation of low U_r region, extremely intensified roll-ups of the separated shear layer are observed near the leading edges of the cross-section. This might be due to a lack of turbulence diffusion inherent in the two-dimensional analysis. Further studies will be required to clarify the reason.

Fig. 21 shows an unsteady pressure distribution at $U_r=1.42$ where torsional vortex-induced vibration occurs. The numerical results agree well with the experiment by Shiraishi et al. (1985) and the three-dimensional numerical analysis by Seto et al. (1997).

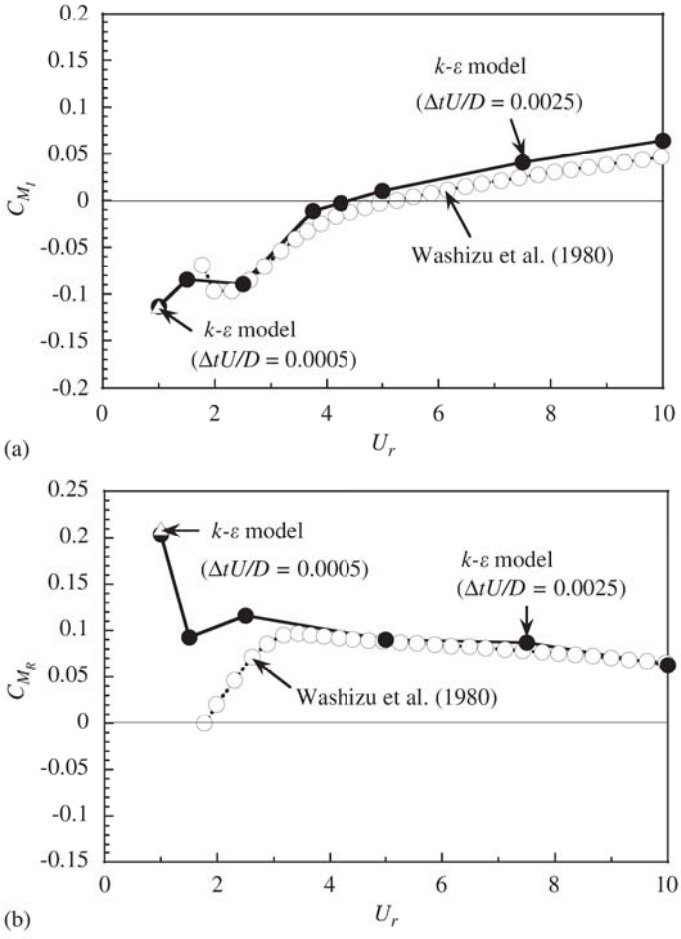

Fig. 20. Unsteady pitching-moment coefficients of a $B/D=4$ cross-section in torsional mode with $\theta_0=3.82^\circ$: (a) out-of-phase component and (b) phase.

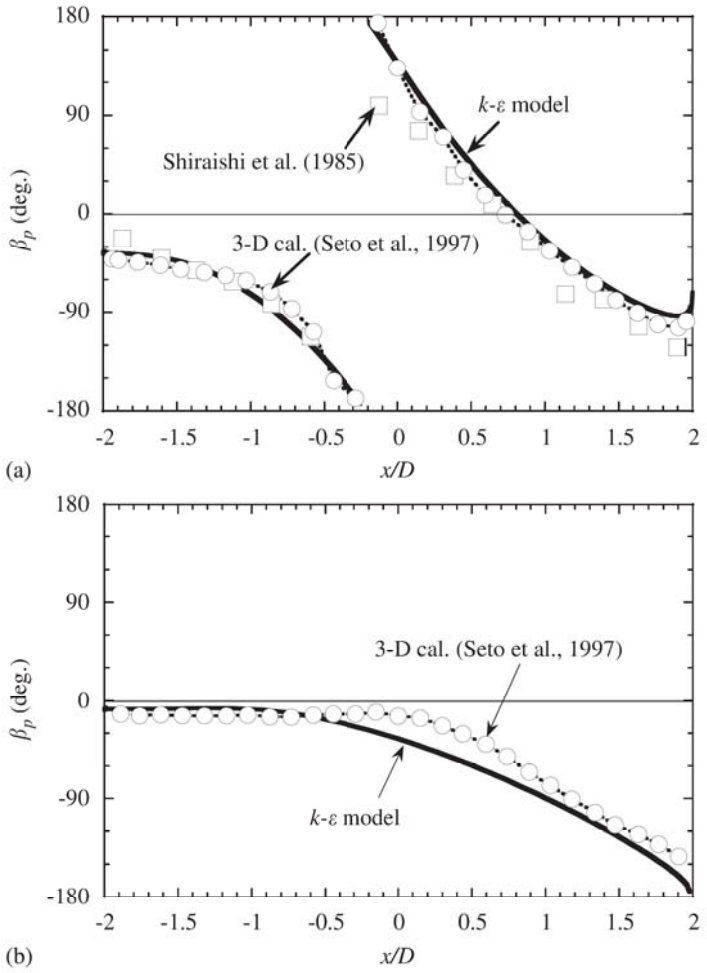

Fig. 21. Phase of fluctuating pressure of a $B/D=4$ cross-section in forced vibration mode with $\theta_0=0.52°$: (a) $U_r=1.42$ and (b) $U_r=6$.

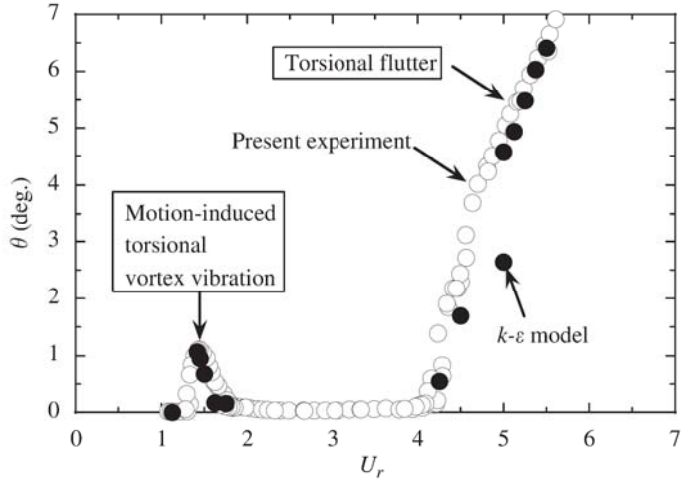

Fig. 22. Normalized response of a $B/D=4$ cross-section in torsional free vibration.

5.4. Simulation of rotationally elastically supported $B/D=4$ cross-section

Fig. 22 compares the torsional vibrations of a $B/D=4$ cross-section of the present numerical simulation and the experiment. Although the damping decrement shows an amplitude dependency as indicated in Fig. 5, in this simulation it is kept as a constant $h=0.283\%$, i.e. $Sc=2I\delta/(\rho B^2D^2)=5.3$. Although the simulated results for $4<U_r<5$ are slightly different from the experimental results, numerical analysis successfully simulates the torsional vortex-induced vibration at $U_r=1.25$ and torsional flutter at $U_r=4$.

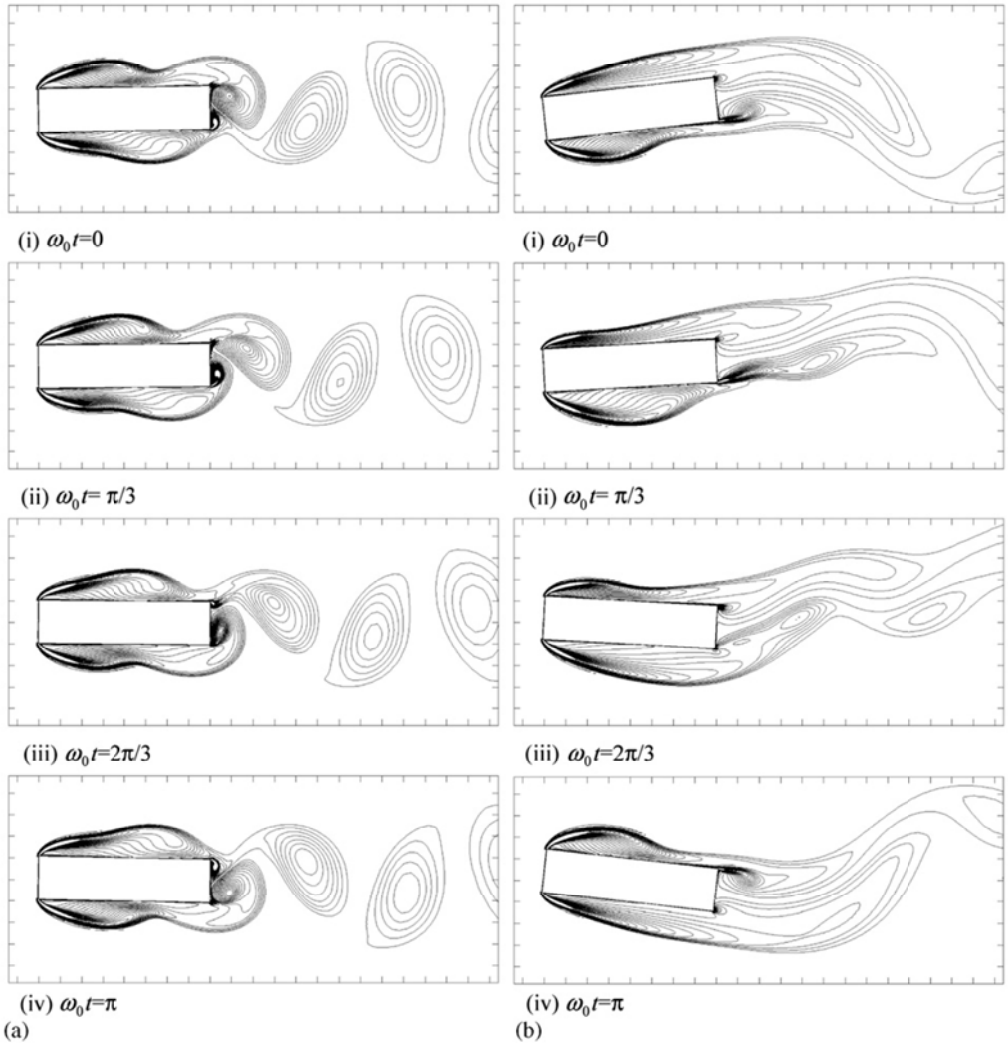

Fig. 23. Instantaneous vorticity field of a $B/D=4$ cross-section in torsional free vibration: (a) torsional vortex-induced-vibration ($U_r=3$) and (b) torsional flutter ($U_r=6.25$).

Fig. 23 shows instantaneous vorticity fields for torsional vortex-induced vibration and torsional flutter for a half cycle of the motion. In the motion-induced-vortex vibration, a separated shear layer from a leading edge which rolls up into a vortex is merged with the secondary vortex formed at the trailing edge and is shed into the wake. In the torsional flutter, no apparent vortex is observed. A separation bubble is generated when the section rises up its head and gradually covers the whole of the side surface.

6. Conclusion

This paper has studied the predictability of the unsteady two-dimensional k–ε model for aerodynamic instabilities for $B/D=2$ and 4 cross-sections. As a result, one-degree-of-freedom transverse and torsional motions were successfully simulated. Results are summarized as follows.

(1) Onset velocities and response amplitudes of vortex-induced vibration for $B/D=2$ and $B/D=4$ were well predicted with respect to both transverse and torsional motions by this analysis.
(2) With respect to torsional flutter, its onset velocity was well predicted quantitatively for both $B/D=2$ and $B/D=4$. Response amplitudes were globally simulated, but were partially inconsistent with the experiment.
(3) With respect to galloping, in this paper only up to a reduced velocity $U_r=12$, which is transition from vortex-induced vibration, was calculated. However, it was well predicted for relatively small mass damping ratio.

In computational fluid dynamics, various kinds of numerical schemes, turbulence models and near wall boundary treatments have been proposed in order to solve high-Reynolds-number flow more accurately and stably. In this paper, with a suitable choice and combination, without any modification of their parameters, various kinds of aerodynamic instabilities caused by vortex were successfully simulated.

Since further research is required on various kinds of complicated cross-sections of practical structures, as an application of the model in the present stage, it is desirable to use it with experimental results to account for their aerodynamic mechanism. Since two-dimensional calculation is fast, it enables the mechanical parameters to be changed over a broad range. As a result, it is possible to grasp global characteristics of aerodynamic instability. Furthermore, since motion, flow field, pressure and aerodynamic forces are obtained simultaneously, which is difficult in the experiments, it is possible to gain a deeper insight into the mechanism. Therefore, this model may be effective, for example, as a tool for optimization of aerodynamic motion mitigation.

Acknowledgment

The authors thank emeritus Prof. Masaru Matsumoto of Kyoto University for his useful suggestions and encouragement in these studies.

Appendix A. Normalized work by unsteady pressure

Work done by fluctuating pressure acting on a point on the upper surface of the cross-section for a cycle of oscillation is expressed as

$$W = -\oint p \cdot dy = -\oint p\dot{y}dt. \tag{A.1}$$

Although $p(t)$ has many frequency components, if the motion of a structure is sinusoidal with circular frequency ω_m, due to the orthogonality of the trigonometric function only the ω_m component is extracted. Therefore,

$$W = -\oint p_m(t)\dot{y}_m dt, \tag{A.2}$$

where $p_m(t)$ is the ω_m component in $p(t)$ and y_m is forced displacement which are defined as

$$P_m(t) = \frac{1}{2}\rho U_0^2 \Re[(C_{p_R} + iC_{p_I})\exp^{i\omega_m t}] = \frac{1}{2}\rho U_0^2 (C_{p_R}\sin\omega_m t + C_{p_I}\cos\omega_m t)\,, \tag{A.3}$$

$$y_m = (x\sin\theta_0)\sin\omega_m t, \tag{A.4}$$

in which θ_0 is amplitude of angular displacement. Therefore the work is obtained as

$$\begin{aligned} W &= -\frac{1}{2}U_0^2\omega_m \int_0^{2\pi/\omega_m} C_{p_I}\cos\omega_m t(x\sin\theta_0)\cos\omega_m t\,dt \\ &= -\frac{1}{2}U_0^2\omega_m \int_0^{2\pi/\omega_m} |C_{p_m}|\sin\beta_p(x\sin\theta_0)\cos^2\omega_m t\,dt \\ &= -\frac{1}{2}U_0^2\frac{\omega_m}{2}|C_{p_m}|\sin\beta_p(x\sin\theta_0)\int_0^{\frac{2\pi}{\omega_m}}(1+\cos 2\omega_m t)dt \\ &= -\frac{1}{2}U_0^2\pi|C_{p_m}|\sin\beta_p(x\sin\theta_0)\,, \end{aligned} \tag{A.5}$$

Hence, normalized work done by fluctuating pressure acting on a point on the upper surface of the cross-section for a cycle of oscillation is expressed as

$$W_r = \frac{W}{(1/2)\rho U_0^2 D} = -\pi|C_{p_m}|\sin\beta_p\left(\frac{x}{D}\sin\theta_0\right). \tag{A.6}$$

References

Harlow, F.H., Welch, J.E., 1965. Numerical calculation of time dependent viscous incompressible flow with free surface. Physics of Fluids 8, 2182–2189.
Itoh, Y., Tamura, T., 2002. Galloping mechanism of a rectangular cylinder. Journal of Wind Engineering and Industrial Aerodynamics 90 (4–5), 377–394.
Kato, M., 1997. 2-D turbulent flow analysis with modified k–ε around a stationary square cylinders and vibrating one in the along and across wind direction. Structural Engineering/Earthquake Engineering, JSCE I-41 (577), 217–230 (in Japanese).
Kato, M., Launder, B.E., 1993. The modeling of turbulent flow around stationary and vibrating square cylinders. In: Proceedings of the Ninth Symposium on "Turbulent Shear Flows", Kyoto, Japan.
Kawamura, T., Kuwahara, K., 1984. Computation of High Reynolds Number Flow Past 2D Square Circular Cylinder with Surface Roughness. AIAA Paper 84-0340.
Kubo, Y., Hirata, K., Mikawa, K., 1992. Mechanism of aerodynamic vibrations of shallow bridge girder sections. Journal of Wind Engineering and Industrial Aerodynamics 41–44, 1297–1308.
Kuroda, S., 2000. Numerical computation of unsteady aerodynamic forces for long-span bridge with two-equation turbulence model. Structural Engineering/Earthquake Engineering, JSCE 654/I-52, 377–387 (in Japanese).
Larsen, A., Walther, J.H., 1998. Discrete vortex simulation of flow around five generic bridge deck sections. Journal of Wind Engineering and Industrial Aerodynamics 77&78, 591–602.
Matsumoto, M., Daito, Y., Yoshizumi, F., Ichikawa, Y., Yabutani, T., 1997. Torsional flutter of bluff bodies. Journal of Wind Engineering and Industrial Aerodynamics 69–71, 871–882.

Miyata, T., Miyazaki, M., Yamada, H., 1983. Pressure distribution measurements for wind induced vibrations box girder bridges. Journal of Wind Engineering and Industrial Aerodynamics 14, 419–430.
Miyazaki, M., 1982. Suppression of wind oscillation of long span box girder decks—view from characteristics of pressure in motion. In: Proceedings of the Seventh National Symposium on Wind Engineering, Tokyo Japan, pp. 187–194 (in Japanese).
Mizota, T., Nakamura, Y., 1974. Wind tunnel blockage effects on drag coefficient and wind-induced vibration. In: Proceedings of the Third Symposium on Wind Effects on Structures in Japan, Tokyo Japan, pp. 201–208 (in Japanese).
Nakamura, Y., Mizota, T., 1975. Torsional flutter of rectangular prisms. Journal of Engineering Mechanics Division, Proceedings of the American Society of Civil Engineering 101 (EM2), 125–142.
Nomura, T., 1994. ALE finite element computations of fluid–structure interaction problems. Computer Methods in Applied Mechanics and Engineering 112 (1–4), 291–308.
Norris, L.H., Reynolds, W.C., 1975. Report No. FM-10. Department of Mechanical Engineering, Stanford University, Stanford, CA, USA.
Païdoussis, M.P., Price, S.J., Langre, E.de, 2011. Fluid–Structure Interactions—Cross-Flow-Induced Instabilities. Cambridge University Press (pp. 66–77).
Parkinson, G.V., Wawzonek, M.A., 1981. Some considerations of combined effects of galloping and vortex resonance. Journal of Wind Engineering and Industrial Aerodynamics 8, 135–143.
Rodi, W., 1991. Experience with Two-Layer Models Combining the k–ε Model with a One-Equation Model Near the Wall. AIAA-91-0216.
Sarwar, M.W., Ishihara, T., Shimada, K., Yamasaki, Y., Ikeda, T., 2008. Prediction of aerodynamic characteristics of a box girder bridge section using the LES turbulence model. Journal of Wind Engineering and Industrial Aerodynamics 96, 1895–1911.
Seto, T., Itoh, Y., Tamura, T., 1997. 3D computation for aerodynamic characteristics of a forced oscillating in torsional mode rectangular cylinder. In: Proceedings of the Summaries of Technical Papers of the Annual Meeting. Architectural Institute of Japan, Structure-I 20099, pp. 197–198 (in Japanese).
Shimada, K., 1995. Numerical analysis for the vortex-induced oscillation of prism with an elongated rectangular cross section (motion-induced vortex oscillation of 2D prism with B/D=2 cross section). Transactions of the Japan Society of Mechanical Engineers C 61 (585), 1776–1783 (in Japanese).
Shimada, K., Ishihara, T., 2001. Application of a modified k–ε model to the prediction of aerodynamic characteristics of rectangular cross-section cylinders. Journal of Fluids and Structures 16 (4), 465–485.
Shirai, S., Ueda, T., 2003. Aerodynamic simulation by CFD on flat box girder of super-long-span suspension bridge. Journal of Wind Engineering and Industrial Aerodynamics 91, 279–290.
Shiraishi, N., Matsumoto, M., 1982. On vortex-induced oscillations of bluff cross sections used for bridge structures. Proceedings of the Japan Society of Civil Engineers 322, 37–50 (in Japanese).
Shiraishi, N., Matsumoto, M., Shirato, H., Kishi, A., 1985. On separated flow characteristics around bluff body and its aerodynamic response. Disaster Prevention Research Institute Annals B-1 (28), 389–406 (in Japanese).
Takeda, K., Kato, M., 1992. Wind tunnel blockage effects on drag coefficient and wind-induced vibration. Journal of Wind Engineering and Industrial Aerodynamics 42, 897–908.
Takeuchi, T., Matsumoto, M., 1992. Aerodynamic response characteristics of rectangular cylinders in tandem arrangement. Journal of Wind Engineering and Industrial Aerodynamics 41–44, 565–575.
Tamura, T., Kuwahara, K., 1992. Numerical study on aerodynamic instability of oscillating rectangular cylinders. Journal of Wind Engineering and Industrial Aerodynamics 41–44, 253–254.
Tamura, T., Itoh, Y., 1997. Three-dimensional vortical flows around a bluff cylinder in unstable oscillations. Journal of Wind Engineering and Industrial Aerodynamics 67&68, 141–154.
Tamura, T., Itoh, Y., 1998. Effects of mass ratio and damping factor on response of unstable oscillations. Journal of Structural and Construction Engineering. Transactions of AIJ 504, 15–21 (in Japanese).
Tamura, Y., Matsui, G., 1979. Wake-oscillator model for vortex induced oscillation of circular cylinder. In: Proceedings of the Fifth International Conference on Wind Engineering, Fort Collins, Colorado, USA, pp. 1085–1094.
Tamura, Y., Shimada, K., 1987. A mathematical model for the transverse oscillations of square cylinders. In: Proceedings of the International Conference on Flow Induced Vibrations, Bowness-Windermere, England, 12-14, PAPER F4, pp. 267–275.
Washizu, K., Ohya, A., Otsuki, Y., Fujii, K., 1978. Aeroelastic instability of rectangular cylinders in a heaving mode. Journal of Sound and Vibration 59 (2), 195–210.
Washizu, K., Ohya, A., Otsuki, Y., Fujii, K., 1980. Aeroelastic instability of rectangular cylinders in a torsional mode. Journal of Sound and Vibration 72 (4), 507–521.